



# Methane in Analogs of Young Directly Imaged Exoplanets

Brittany E. Miles<sup>1</sup>, Andrew J. Skemer<sup>1</sup>, Travis S. Barman<sup>2</sup>, Katelyn N. Allers<sup>3</sup>, and Jordan M. Stone<sup>4</sup>

<sup>1</sup>Department of Astronomy and Astrophysics, University of California, Santa Cruz, CA, USA; [bmiles@ucsc.edu](mailto:bmiles@ucsc.edu)

<sup>2</sup>Lunar and Planetary Lab, University of Arizona, Tucson, AZ, USA

<sup>3</sup>Department of Physics and Astronomy, Bucknell University, Lewisburg, PA, USA

<sup>4</sup>Steward Observatory, University of Arizona, Tucson, AZ, USA

Received 2018 August 23; revised 2018 September 25; accepted 2018 October 5; published 2018 December 6

## Abstract

We present detections of methane in  $R \sim 1300$ ,  $L$ -band spectra of VHS 1256 b and PSO 318.5, two low-gravity, red, late L dwarfs that share the same colors as the HR 8799 planets. These spectra reveal shallow methane features, which indicate VHS 1256 b and PSO 318.5 have photospheres that are out of chemical equilibrium. Directly imaged exoplanets usually have redder near-infrared colors than the field-age population of brown dwarfs on a color–magnitude diagram. These objects along the L-to-T transition show reduced methane absorption and evidence of photospheric clouds. Compared to the  $H$ - and  $K$ -bands,  $L$ -band ( $3\text{ }\mu\text{m}$ – $4\text{ }\mu\text{m}$ ) spectroscopy provides stronger constraints on the methane abundances of brown dwarfs and directly imaged exoplanets that have similar effective temperatures to L-to-T transition objects. When combined with near-infrared spectra, the  $L$ -band extends our conventional wavelength coverage, increasing our understanding of atmospheric cloud structure. Our model comparisons show that relatively strong vertical mixing and photospheric clouds can explain the molecular absorption features and continua of VHS 1256 b and PSO 318.5. We also discuss the implications of this work for future exoplanet-focused instruments and observations with the *James Webb Space Telescope*.

**Key words:** brown dwarfs – stars: individual (VHS J125601.92–125723.9b, PSO J318.5338–22.8603) – planets and satellites: atmospheres – planets and satellites: gaseous planets

**Supporting material:** data behind figure

## 1. Introduction

Methane ( $\text{CH}_4$ ) is fundamental to our understanding of planet formation and other processes that influence the composition of an exoplanet’s atmosphere (Barman et al. 2011a; Öberg et al. 2011). Methane is detected on the majority of solar system planets, represents a large fraction of the carbon budget in gas giant planets, and is a significant greenhouse gas produced by biological and geological processes on Earth (Lunine 1993; Karkoschka 1994; Keppler et al. 2006; Guzmán-Marmolejo & Segura 2015). Detecting and constraining methane is extremely important for characterizing exoplanets as a whole.

Current directly imaged gas giants like the HR 8799 planets (Marois et al. 2008, 2010) show much less methane in their  $H$ -band spectra than is seen in the majority of similar-temperature field brown dwarfs (Bowler et al. 2010; Barman et al. 2011a). Most directly imaged exoplanets also have red near-infrared colors compared to most field brown dwarfs, especially near the L-to-T transition (see Figure 1; Liu et al. 2016). The L-to-T transition is both an evolutionary transition and a region of the near-infrared color–magnitude diagram where (1) cloud properties rapidly alter the near-infrared colors of brown dwarfs by several magnitudes over a small temperature range, and (2) the dominant carbon-bearing, photospheric gas transitions from carbon monoxide (CO) to methane ( $\text{CH}_4$ ; Burrows et al. 1997, 2006; Ackerman & Marley 2001; Burgasser et al. 2002; Geballe et al. 2002; Tsuji & Nakajima 2003; Knapp et al. 2004; Saumon & Marley 2008). The relatively red near-infrared colors of directly imaged exoplanets have primarily been explained by lingering photospheric clouds composed of silicate and iron condensates (Currie et al. 2011; Madhusudhan et al. 2011; Marley et al. 2012). The lack of methane is thought to be the result of disequilibrium chemistry,

driven by vertical mixing interchanging cool  $\text{CH}_4$ -rich gas with warmer CO-rich gas (Barman et al. 2011a, 2011b; Zahnle & Marley 2014).

To understand cloud properties and atmospheric mixing in exoplanets, broad wavelength coverage is essential for breaking degeneracies. Atmospheric models that only consider clouds can reproduce the near-infrared ( $0.8$ – $2.3\text{ }\mu\text{m}$ ) colors of exoplanets, but underpredict their fluxes from  $3$  to  $4\text{ }\mu\text{m}$  (Hinz et al. 2010; Barman et al. 2011b, 2015; Skemer et al. 2012, 2014). Various studies have been able to get better fits to  $1\text{ }\mu\text{m}$ – $5\text{ }\mu\text{m}$  photometry and spectroscopy of 2MASS J 1207334–393254b (2MASS 1207 b; Chauvin et al. 2004) and the HR 8799 planets by including the effects of iron and silicate clouds, patchy clouds, and non-equilibrium chemistry (Marois et al. 2008, 2010; Hinz et al. 2010; Barman et al. 2011a, 2011b, 2015, 2015; Currie et al. 2011, 2014; Skemer et al. 2011; Marley et al. 2012; Skemer et al. 2012, 2014; Konopacky et al. 2013).

Currently, our understanding of directly imaged exoplanet atmospheres is limited by data quality. Directly imaged exoplanets are difficult to observe because they are faint compared to the glare of their much brighter host stars. Young, free-floating, and wide-separation planetary-mass objects often share the same color space as directly imaged gas giant exoplanets (Faherty et al. 2013; Liu et al. 2016). These objects are significantly easier to study in detail and provide insight into the atmospheric properties of bona fide gas giant exoplanets.

In this study, we present  $L$ -band ( $3$ – $4\text{ }\mu\text{m}$ ) spectra of two exoplanet analogs, VHS J125601.92–125723.9b (VHS 1256 b; Gauza et al. 2015) and PSO J318.5338–22.8603 (PSO 318.5; Liu et al. 2013). The opacity of  $\text{CH}_4$  dominates over all other gases within the  $L$ -band (peaking at  $\sim 3.3\text{ }\mu\text{m}$ ; see Morley et al. 2014; Yurchenko & Tennyson 2014), allowing for an unambiguous

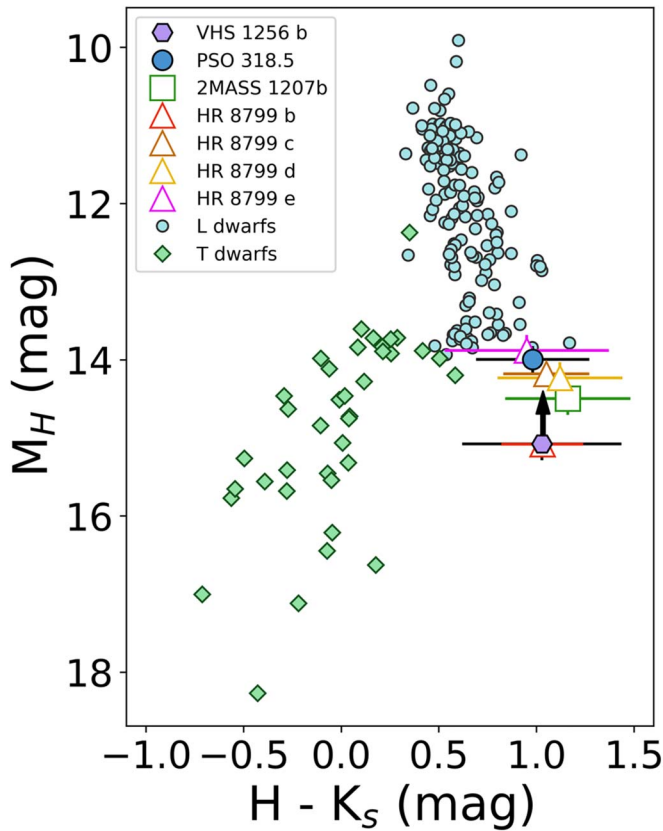


**Figure 1.** Color-magnitude diagram of L (blue circles) and T (light green diamonds) dwarfs using measured and synthesized 2MASS magnitudes compiled in Dupuy & Liu (2012). The HR 8799 planets are plotted as triangles with colored edges (Marois et al. 2008, 2010; Metchev et al. 2009; Skemer et al. 2012). 2MASS 1207 b, a very young, low-mass companion, is plotted as a square with green edges (Chauvin et al. 2004). VHS 1256 b is plotted as a lavender hexagon, and PSO 318.5 is plotted as a blue circle. The distance to VHS 1256 b is not well constrained; therefore, the black arrow represents a range of possible absolute magnitudes.

detection, even at low abundances. VHS 1256 b and PSO J318.5 are both low-gravity objects that have similar colors to the HR 8799 planets (Figure 1) and show no near-infrared CH<sub>4</sub> absorption.

VHS 1256 b is a wide companion (8'' separation) to a late M dwarf binary system (Stone et al. 2016), making it accessible to long slit spectroscopy. The age of the VHS 1256 system is not well known; however, VHS 1256 b's weak absorption from neutral gases (Na and K) and collisionally induced absorption from hydrogen indicates a low surface gravity, which implies youth (Gauza et al. 2015). Model fits to the optical to mid-infrared photometry of VHS 1256 b suggest a very cloudy atmosphere (Rich et al. 2016). PSO J318.5 is a free-floating object that is a member of the  $\beta$  Pictoris moving group, making it about 20–25 Myr old (Allers et al. 2016). The time series photometry and near-infrared spectra of PSO 318.5 also suggest a cloudy atmosphere (Biller et al. 2015, 2018).

In Sections 2 and 3, we present *L*-band observations and reductions of VHS 1256 b and PSO J318.5. In Section 4, we quantify the significance of the CH<sub>4</sub> features and fit our *L*-band spectra and published near-infrared spectra with atmospheric models. We discuss the astrophysical ramifications of our results and future observations with ground-based, high-contrast imagers and the *James Webb Space Telescope* (JWST) in Section 5. We summarize our results in Section 6.

## 2. Observations

We observed VHS 1256 b and PSO 318.5 on UT 2016 June 19 during photometric conditions using the NIRSPEX spectrograph (McLean et al. 1998), an instrument on the Keck II Telescope on Maunakea. NIRSPEX was set up in low-resolution mode with the *KL* filter and a 42'' by 0.570'' slit. Two grating positions were used to achieve a wavelength coverage from 2.9 to 4.4  $\mu$ m with a resolution of 1300 (in low-resolution mode, NIRSPEX has a nominal resolution of  $\sim$ 2500 with a 0.380'' slit). Between 4.2 and 4.4  $\mu$ m, the atmospheric transmission is zero, and the *KL* filter only transmits out to 4.2  $\mu$ m. Our observations are background limited due to the high thermal emission from Earth's atmosphere. An integration time of 0.5 s with 120 co-adds was chosen for each spectral image. The spectral images were taken in an ABBA nod pattern. Telluric calibrations were taken before and after every two or three ABBA sequences for both science targets. AOV and A1V stellar spectra were taken at the same airmass as the science targets and used as telluric calibrators. The mean precipitable water vapor for our observations was 1.3 mm, and the standard deviation over the night was 0.06 mm. There were only smooth changes in water vapor over each science observation block. The slit was not aligned to the parallactic angle for every observation over the course of the night; however, atmospheric dispersion across the *L*-band is negligible. A summary of all NIRSPEX observations is listed in Table 1.

## 3. Data Reduction

### 3.1. Removing NIRSPEX Detector Artifacts and Background Subtraction

Bad pixels were identified by looking at the entire night of spectral images for anomalous values (negative or extremely low/high values across sky lines) appearing at the same position. Bad pixels in the spectral images are replaced by the average of the surrounding pixels. A–B pair nod subtraction is done to eliminate the majority of the sky lines from the traces in the calibrator and science spectral images. Each A–B pair produces a spectral image with a positive and a negative trace. The top-right quadrant (redder half in low-resolution mode) of NIRSPEX's detector has pattern noise that appears as a horizontal row of increased noise every eight pixels that is primarily along the spatial direction. The pattern noise response is always smaller than the sky emission and calibrator stars but changes quickly between exposures, making it difficult to remove with A–B pair nod subtraction. The width of the pattern noise was one pixel for all observations of VHS 1256 b. The first block of PSO 318.5 data in the 32°76 grating setting has a one-pixel-wide pattern noise. The pattern noise width in the last three blocks of the same setting increased to a width of two pixels. The first half and last half of the 34°19 grating setting PSO 318.5 data have a one- and two-pixel-wide pattern noise, respectively. This pattern noise was addressed in the A–B pair-subtracted spectral images for each pixel by doing a linear interpolation using the pixel above and the pixel below from the affected rows.

### 3.2. Spectral Image Rectification and Residual Sky Subtraction

The spectral traces are curved in the A–B pair-subtracted spectral images and are rectified before extraction. Centroids are fit along the traces of the calibrator star spectral images to estimate the deviation from a straight line and create the spatial rectification map. The spatial rectification map is applied to an A + B image of the calibrator star, where the sky lines are used to create a

**Table 1**  
Summary of the UT 2016 June 19 NIRSPEC Observations

Science Target	Grating Angle (°)	Wavelength Coverage ( $\mu\text{m}$ )	AB Pairs (N)	Science Airmass	Telluric Calibrator	AB Pairs (N)	Telluric Airmass
VHS 1256 b	32.76	2.9–3.8	6	1.24	HIP 63109	3	1.24
VHS 1256 b	32.76	2.9–3.8	4	1.42	HIP 62096	2	1.42
VHS 1256 b	34.19	3.5–4.4	6	1.23	HIP 63109	2	1.29
VHS 1256 b	34.19	3.5–4.4	6	1.39	HIP 62096	2	1.50
PSO 318.5	32.76	2.9–3.8	6	1.72	HIP 101384	2	1.72
PSO 318.5	32.76	2.9–3.8	4	1.38	HIP 99592	2	1.40
PSO 318.5	32.76	2.9–3.8	6	1.35	HIP 104810	2	1.36
PSO 318.5	32.76	2.9–3.8	4	1.33	HIP 109775	2	1.43
PSO 318.5	34.19	3.5–4.4	6	1.68	HIP 101384	2	1.64
PSO 318.5	34.19	3.5–4.4	4	1.37	HIP 99592	2	1.40
PSO 318.5	34.19	3.5–4.4	6	1.35	HIP 104810	2	1.36
PSO 318.5	34.19	3.5–4.4	4	1.32	HIP 109775	2	1.41

**Note.** The reported airmasses of the science target and calibrator observations are median values. Our observations extend out to 4.4  $\mu\text{m}$  in wavelength coverage, but the transmission of the *KL* filter beyond 4.2  $\mu\text{m}$  is zero. Each nod consists of 120 co-adds of 0.5 second exposures.

second rectification map for the wavelength direction. Creating rectification maps from the science targets is difficult because their traces are extremely faint. Therefore, the two spatial and spectral rectification maps calculated from the calibrator star are applied to the A–B images of the calibrator star and the A–B images of the associated science target. After nod subtracting and rectifying the calibrator and science images, there is still excess sky to be removed. At each row along the entire wavelength direction, the median of the pixels along the spatial direction is subtracted off.

### 3.3. Wavelength Solution

The wavelength solution is calculated by fitting a second-order polynomial to the sky emission lines along the wavelength direction of the spatially and spectrally rectified A + B calibrator images. The spectral features are identified by referencing a smoothed model of the Maunakea sky<sup>5</sup> to a resolution of 1300, matching the data. For the 32°76 grating setting, 18 benchmark features were used to estimate the wavelength solution. For the 34°19 grating setting, six benchmark features were used. We estimate the uncertainty in the wavelength solution by taking the difference between the initial wavelengths of the benchmark lines and the final wavelengths of the benchmark lines after the wavelength solution has been assigned. On average, there is a 0.4 pixel or  $2.5 \times 10^{-4} \mu\text{m}$  offset, but it is not significant for our analysis and is addressed by binning the spectra.

### 3.4. Spectral Extraction and Error Estimation

To find the centers and widths of the traces, we take the mean of the fully rectified A–B spectral images and sum along the wavelength direction. A Gaussian is fit to the positive and negative trace profiles, and the standard deviation of the profile is used to estimate the optimal radius ( $1.5852\sigma$ ,<sup>6</sup> typical radius was 3.5 pixels) for the boxcar extraction. To estimate the error at every wavelength element, we take the nearest 25 pixels to the left and right of the trace centroid, mask out the trace within the extraction radius, fit a first-order polynomial to the counts and pixel positions, then take the variance of the residual of the fit

from the row counts. The goal of this is to capture the average noise away from some baseline profile, which is not necessarily constant across an entire wavelength. The variance of the residual is multiplied by the square root of the extraction width to get an error at each wavelength element.

### 3.5. Telluric and Relative Flux Calibration

The calibrators and the science targets will have their spectra influenced by the transmission of Earth’s atmosphere, which includes absorption from gaseous methane. The absorption of Earth’s atmosphere is addressed by dividing the raw science spectrum by a telluric calibrator spectrum that has a known response, such as a blackbody. To account for the transmission of Earth’s atmosphere, each science trace is telluric-calibrated by dividing the extracted trace by an A0 or A1 star.

The errors of the telluric-calibrated science spectrum are calculated with standard error propagation, using error information from the extracted science trace and the telluric spectrum. The background from the science trace is the dominant source of error. The telluric-calibrated line of the science target is then multiplied by Planck’s law at the appropriate temperature based on the spectral type of the calibrator star. We have two telluric-calibrated spectra for every A–B image. Our science observations were bracketed by A0 and A1 stars at similar airmasses for good telluric correction, which is important especially around the methane feature at 3.3  $\mu\text{m}$ . Even though Earth’s transmission is low near 3.3  $\mu\text{m}$ , we still have significant signal for our calibrators (Figure 2).

To quantify the quality of the telluric calibration, we extract the calibrator spectra taken before and after each science target block, normalize by the median, and then divide the “before” calibrator by the “after” calibrator. The ratio of the normalized “before” calibrator to the normalized “after” calibrator should be unity, but there are deviations, especially where the atmospheric transmission is very low. The deviation from one is interpreted as a percentage error that is included in the error of the final spectrum.

For each science target, the telluric- and relative flux-calibrated spectra from each observational block are normalized by the median value. All of the normalized data points from each observational block are combined, reordered by wavelength, and binned down to 512 pixels using a weighted average. The ratios of the “before” and “after” calibrators are reordered and binned down using the same weights. The final

<sup>5</sup> [www.gemini.edu/sciops/telescopes-and-sites/observing-condition-constraints/ir-background-spectra](http://www.gemini.edu/sciops/telescopes-and-sites/observing-condition-constraints/ir-background-spectra)

<sup>6</sup> <http://wise2.ipac.caltech.edu/staff/fmasci/GaussApRadius.pdf>



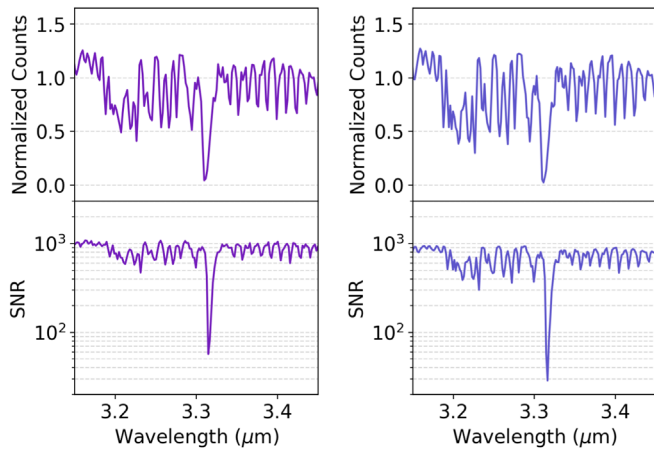


**Figure 2.** Top: the average telluric spectra for VHS 1256 b (left) and PSO 318.5 (right), centered on the peak of the Q-branch ( $3.3 \mu\text{m}$ ) methane feature. Bottom: the signal-to-noise ratio (S/N) of the average telluric spectra for VHS 1256 b (left) and PSO 318.5 (right). At  $3.31 \mu\text{m}$ , the atmospheric transmission is fairly low; however, the telluric spectra have an S/N of 57 and 29, respectively, in these troughs.

normalized spectra for VHS 1256 b and PSO 318.5 along with the telluric calibration ratios are shown in Figure 3.

### 3.6. Absolute Flux Calibration

Unlike A-type stars, brown dwarfs are not well approximated by a blackbody due to absorption from various molecules. Therefore, it is not appropriate to scale a normalized spectrum by a photometry point at the effective wavelength of a given filter. To find a better scale factor ( $D$ ) by which to multiply the normalized science spectrum, we first solve for the total number of photons through a filter (and sky transmission if necessary) for a flux-calibrated Vega spectrum (Rieke et al. 2008) and the normalized science spectrum.

The total number of photons ( $N$ ) measured within a filter covering a wavelength range from  $\lambda_1$  to  $\lambda_2$  can be approximated by

$$N \propto \sum_{\lambda_1}^{\lambda_2} \frac{F_{\lambda} T_{\lambda} A \tau_{\text{exp}} \lambda \Delta \lambda}{hc}, \quad (1)$$

where  $h$  and  $c$  are the Planck constant and the speed of light, respectively. The transmission through the sky and/or telescope is  $T_{\lambda}$ , the area of the telescope aperture is  $A$ , and the exposure time of the measurement is  $\tau_{\text{exp}}$ .

For one instrument configuration, the ratio of counts from the normalized science target and Vega should be proportional. The scale factor  $D$  is then equal to

$$D = \frac{N_{\text{sci}}}{N_{\text{vega}}} \frac{\sum_{\lambda_1}^{\lambda_2} F_{\lambda, \text{vega}} T_{\lambda} \lambda \Delta \lambda_{\text{vega}}}{\sum_{\lambda_1}^{\lambda_2} F_{\lambda, \text{sci}} T_{\lambda} \lambda \Delta \lambda_{\text{sci}}}. \quad (2)$$

The ratio of science counts to Vega counts can be calculated using the magnitude of the science target within a given filter. To calculate the number of photons that pass through the sky (if relevant) and a filter, the transmission curves are binned down to the resolution of the spectra and then interpolated onto the same wavelengths.

The VHS 1256 b  $L$ -band spectrum is flux-calibrated using the Subaru Infrared Camera and Spectrograph (IRCS)  $L'$  photometry point from Rich et al. (2016). PSO 318.5 has a *Wide-field*

*Infrared Survey Explorer* (WISE; Wright et al. 2010) W1 photometry point, but the W1 filter transmits light blueward of the  $L$ -band spectra. Flux calibrating the PSO 318.5  $L$ -band spectrum is not possible without making assumptions about the continuum shape; therefore, the scale factor ( $D$ ) is allowed to be offset by up to 10% while model fitting.

## 4. Analysis

### 4.1. Detection and Significance of Methane in L-band Spectra

Methane is predicted to be the only significant absorber across the  $L$ -band for  $\sim 1300$  K objects (Morley et al. 2014). Methane absorption becomes deeper and broader through the L-to-T transition, especially around the Q-branch band head of methane that peaks in opacity at  $\sim 3.3 \mu\text{m}$  (Noll et al. 2000; Cushing et al. 2005; Kirkpatrick 2005). VHS 1256 b and PSO 318.5 have features around  $\sim 3.3 \mu\text{m}$  that resemble absorption from methane. Despite their cool photospheric temperatures, these features appear shallow relative to other late L dwarfs and early T dwarfs (Figure 4). Unlike field L dwarfs, the spectral slopes of VHS 1256 b and PSO 318.5 show increasing flux density at longer wavelengths along the  $L$ -band. These slopes resemble the spectral shapes of T dwarfs, but with less methane absorption.

We provide evidence for methane detection by showing that a best-fit line to the data from  $3.2$  to  $3.4 \mu\text{m}$  produces a worse fit than a simple two-line model with a break at the characteristic wavelength ( $\lambda_0$ ) over the same wavelength range. A two-line model does not accurately represent the complex absorption feature of methane, but we want to rule out a smooth continuum before comparing to models with varying methane abundances later in Section 5.3. Methods that quantify absorption, such as the equivalent width or spectral indices, require knowledge of the continuum and that is difficult to account for across the L-to-T transition as methane absorption gets broader. The  $3.2$ – $3.4 \mu\text{m}$  range was chosen for fitting, because that is where methane absorption appears most consistent from the mid-L to mid-T dwarf range (Figure 4). The two-line model  $y(\lambda)$  is described by the function

$$y(\lambda) = \begin{cases} m_1 \lambda + b_1 & \text{for } \lambda \leq \lambda_0 \\ m_2 \lambda + b_2 & \text{for } \lambda > \lambda_0 \end{cases}, \quad (3)$$

and the coefficients are fit using the Markov Chain Monte Carlo method with the Python package *emcee* (Foreman-Mackey et al. 2013). An example of the two-line model can be seen in the best fit for PSO 318.5 in Figure 5.

The relative model quality of the one- and two-line best fits were assessed by a  $\Delta\chi^2$  value and the Akaike Information Criterion (AIC). The difference between the one- and two-line best-fit  $\chi^2$  values produce a  $\Delta\chi^2$  value of 74.6 and 100.3 for VHS 1256 b and PSO 318.5, respectively. For VHS 1256 b, the best-fit two-line model has an AIC of 159.0, and the one-line model has an AIC of 227.7. For PSO 318.5, the best-fit two-line model has an AIC of 181.4, and the one-line model has an AIC of 275.7. For both objects, the two-line model produces a lower AIC and a better quality fit to the data.

The depth parameter ( $\Delta F$ ) is a derived quantity from the two-line model that is the difference between  $y_1(\lambda_0)$  and  $y_2(\lambda_0)$ . A higher value of  $\Delta F$  corresponds to a deeper absorption feature. The posterior distributions of the depth parameter for VHS 1256 b and PSO 318.5 are compared with two L dwarfs, 2MASS J1507–1627 and DENIS J0255–4700, featured in Figure 6. Two other brown dwarfs, 2MASS J1439+1929 (L1)

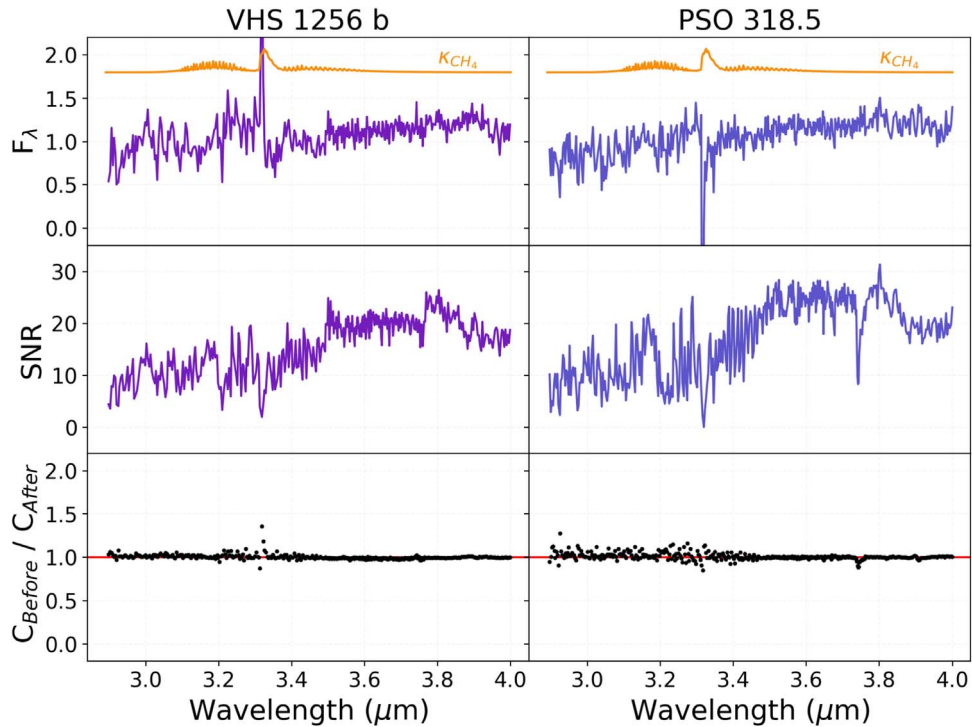


**Figure 3.** Top: normalized flux ( $F_\lambda$ ) plotted against wavelength for VHS 1256 b and PSO 318.5. The opacity of methane is plotted in orange above the spectra in arbitrary units on a linear scale. There is absorption from methane at  $\sim 3.3 \mu\text{m}$  in both objects. Middle: the S/N vs. wavelength for VHS 1256 b and PSO 318.5. Bottom: the “before” calibrator ( $C_{\text{Before}}$ ) divided by the “after” calibrator ( $C_{\text{After}}$ ) combined for all science observations. This is a metric of the telluric calibration quality for each object. Both objects have a standard deviation of 1% over the entire spectrum. Across the peak of the methane feature ( $3.3 \mu\text{m}$ – $3.4 \mu\text{m}$ ), the standard deviation of the telluric ratio is 8% for VHS 1256 b and 5% for PSO 318.5. The telluric ratio deviations are included in our error propagation and reflected in the errors for the S/N plots in the middle panel. The data used to create this figure are available.

and 2MASS J1506+1321 (L3) are also plotted for reference. The mean values of  $\Delta F$  for VHS 1256 b and PSO 318.5 are inconsistent with a straight line ( $\Delta F = 0.0$ ) by  $10.5\sigma$  and  $13.3\sigma$ , respectively. Nearly the entire probability distribution of VHS 1256 b and PSO 318.5’s  $\Delta F$  parameter lies in between the distributions of the 1700 K (L5) brown dwarf and the 1500 K (L8) brown dwarf. This quantitatively shows that VHS 1256 b and PSO 318.5 have methane, but show less methane absorption than hotter brown dwarfs. There is significant overlap between the  $\Delta F$  distributions of VHS 1256 b and PSO 318.5, but the mean  $\Delta F$  of VHS 1256 b is slightly higher.

The depleted methane features of VHS 1256 b and PSO 318.5 are evidence for non-equilibrium chemistry. Previous works have shown that vertical mixing can displace methane from the photosphere with warmer, carbon monoxide dominated gas (Hubeny & Burrows 2007; Zahnle & Marley 2014). In Section 4.3, we further quantify VHS 1256 b’s and PSO 318.5’s methane absorption features and estimate the magnitude of their vertical mixing using custom atmospheric models.

#### 4.2. Published Optical/Near-infrared Studies of VHS 1256 b and PSO 318.5

VHS 1256 b and PSO 318.5 both have optical to mid-infrared photometric measurements and near-infrared spectra that have been published. For our analysis, we applied the absolute flux calibration outlined in Section 3.6 to the normalized near-infrared spectra of VHS 1256 b and PSO 318.5 from Gauza et al. (2015) and Liu et al. (2013). The normalized optical/near-infrared spectrum from Gauza et al. (2015) is broken up into optical/ $J$ ,  $H$ , and  $K$  portions that are flux-calibrated separately using the  $J$ ,  $H$ , and  $K$  VISTA InfraRed CAMera photometry. Two near-infrared

spectra of PSO 318.5 were presented in Liu et al. (2013), but for this work, we do our analysis with the Gemini Near-Infrared Spectrograph (GNIRS) data because it has a higher spectral resolution. The near-infrared spectrum of PSO 318.5 was flux-calibrated using the  $K$ -band MKO photometry (Liu et al. 2013) measured using WFCAM on the UK Infrared Telescope.

Both objects have Two Micron All-Sky Survey (2MASS) measurements, but the 2MASS photometry is not consistent with the VISTA (VHS 1256 b) or MKO (PSO 318.5) photometry. The VISTA and MKO photometry are used for flux calibration because they produce less scatter in the final spectra when scaling by the different infrared photometry points ( $J$ ,  $H$ ,  $K$ ) and are more precise than the 2MASS photometry. Photometric variability studies have been done on PSO 318.5 and similar objects (Biller 2017), and this effect will be discussed later in Section 5.4, although we note that the measured variability cannot explain the photometric discrepancy discussed here.

#### 4.3. Description of Models and Fitting

The models used to fit the data were calculated using a method similar to the one outlined in Barman et al. (2011b) with the PHOENIX atmospheric code and updated  $\text{CH}_4$ ,  $\text{CO}_2$ , and  $\text{NH}_3$  line lists. The intermediate cloud model has a base pressure set by equilibrium chemistry, and the vertical extent of the cloud is parameterized by a pressure value, above which the number density of cloud particles falls off exponentially. The cloud particle sizes follow a log-normal distribution characterized by a median grain size. The composition of the cloud is dependent on equilibrium chemistry, resulting in clouds

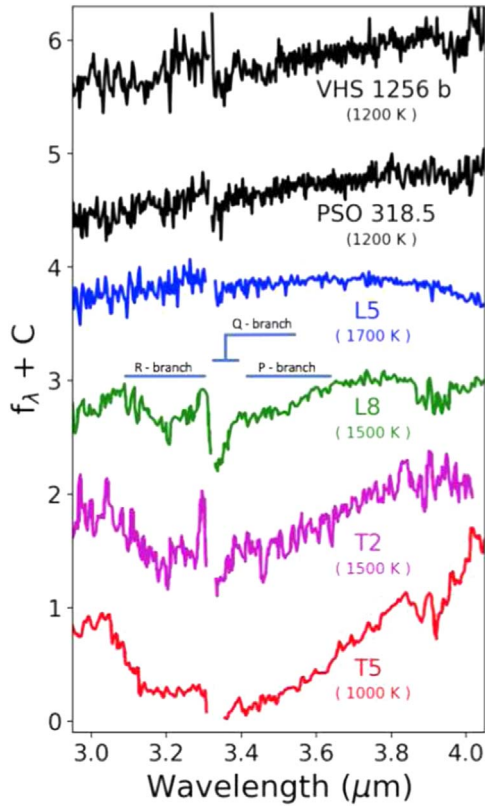


**Figure 4.** Normalized spectra of VHS 1256 b and PSO 318.5 (with S/N < 3 data points removed) along with L-band spectra of 2MASS J1507-1627 (L5), DENIS J0255-4700 (L8), SDSS J1254-0122 (T2), and 2MASS J0559-1404 (T5) from Cushing et al. (2005). All of the spectral type identifications were done in the near-infrared. Each spectrum is normalized at  $3.8 \mu\text{m}$  and offset by an arbitrary constant. The best-fit temperature estimate for VHS 1256 b is from Rich et al. (2016); for PSO 318.5, the estimate is from Liu et al. (2013). The temperatures of the brown dwarfs from Cushing et al. (2005) are estimated using the temperature vs. spectral type relationship derived in Golimowski et al. (2004). The P-, Q-, and R-branch portions of methane absorption are labeled on the L8 brown dwarf. VHS 1256 b and PSO 318.5 have weak Q-branch methane features and show less methane absorption than brown dwarfs of similar temperatures.

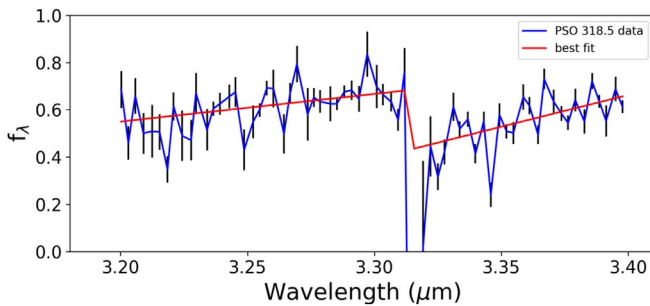


**Figure 5.** To quantify the significance of the methane absorption feature at  $\sim 3.3 \mu\text{m}$ , we fit a one-line model and a two-line model with a characteristic break at  $\lambda_0$  to the data of VHS 1256 b and PSO 318.5. The two-line model produces better fits to our data, showing that the absorption is statistically significant. In this figure, we show the best-fit two-line model (red) to a subset of the PSO 318.5 spectrum (blue).

composed primarily of silicates (e.g., enstatite ( $\text{MgSiO}_3$ ), forsterite ( $\text{MgSiO}_4$ )).

A grid similar to Barman et al. (2011b) was used to fit the parameters of VHS 1256 b and PSO 318.5 to confirm that the inferred temperatures and gravities were similar to previous

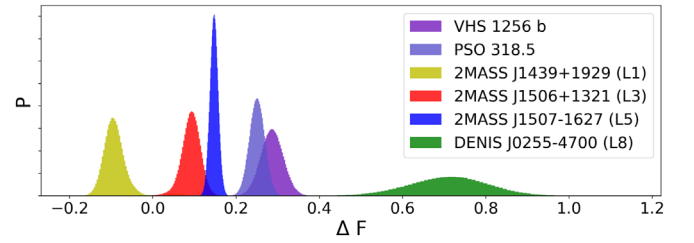


**Figure 6.** Probability distributions of the depth parameter ( $\Delta F$ ) for (left to right) 2MASS J1439+929, 2MASS J1506+1321, 2MASS J1507-1627, PSO 318.5, VHS 1256 b, and DENIS J0255-4700. Positive  $\Delta F$  values correspond to methane absorption. The mean values for each distribution (left to right) are  $-0.02$ ,  $0.09$ ,  $0.15$ ,  $0.25$ ,  $0.34$ , and  $0.66$ . VHS 1256 b and PSO 318.5 have methane absorption distributions that are intermediate between the distributions of 2MASS J1507-1627 (1700 K) and DENIS J0255-4700 (1500 K).

studies of these two objects. Vertical mixing is parameterized by the vertical eddy diffusion coefficient  $K_{zz}$ , which is defined as

$$K_{zz} = \frac{L^2}{\tau_{\text{dyn}}}, \quad (4)$$

where  $\tau_{\text{dyn}}$  is the dynamical timescale and  $L$  is the length scale of diffusion. The length scale in this work is approximately a third of the pressure scale height as outlined in Smith (1998).

Another model grid with slightly finer parameter sampling was created spanning an effective temperature of 1000 K to 2000 K (every 50 K),  $\log g$  from 3.0 to 4.0 (every 0.25 decs), mean grain sizes of (0.5, 1, 2, 3 and  $5 \mu\text{m}$ ), and five different cloud heights. The abundances of these models are assumed to be solar according to Asplund et al. (2009). After an initial best fit was found using  $\chi^2$  values, the cloud distribution, effective temperature, and  $\text{CH}_4$  mixing ratio above the quenching point was tuned for a better fit.

The best-fit model for PSO 318.5 also applies to VHS 1256 b because the objects share similar spectral features. The best-fit model has its structure shown in Figure 7, and the spectrum is shown along with the data in Figure 8. VHS 1256 b and PSO 318.5 each have a best-fit temperature of 1240 K, and a best-fit  $K_{zz}$  of  $10^8 \text{ cm}^2 \text{ s}^{-1}$ . Above the quenching point, the mixing ratio of  $\text{CH}_4$  was increased by two orders of magnitude to  $2.4 \times 10^{-6}$  for PSO 318.5 and  $3.5 \times 10^{-6}$  for VHS 1256 b to get a better fit. From about 1 to 0.1 bar, the abundance of  $\text{CH}_4$  is two orders of magnitude higher in the best-fit non-equilibrium case than in the equilibrium case. Above 0.1 bar, the best-fit non-equilibrium model has one to two orders of magnitude less methane than the equilibrium case (Figure 8, Middle Panel). The photospheres have clouds with a median grain size of  $0.5 \mu\text{m}$ . An increased  $\text{CH}_4$  mixing ratio also implies that a model with a smaller  $K_{zz}$  value could also explain the spectra.

With an assumed distance of 22 pc (Liu et al. 2016), the inferred radius of PSO 318.5 is  $1.3 R_{\text{Jup}}$ , which is consistent with PSO 318.5 being a young, planetary-mass object (Baraffe et al. 1998). With an assumed distance of 17 pc (Stone et al. 2016), the implied radius of VHS 1256 b is  $0.9 R_{\text{Jup}}$ , which is inconsistent with youth (Baraffe et al. 1998). The parallax and photometric distance estimates of the binary host are discrepant (Stone et al. 2016); therefore, there is a large uncertainty on the actual radius of VHS 1256 b. VHS 1256 b has very similar spectral features to PSO 318.5, and to get a similar radius, VHS 1256 b could possibly be as far as 20 pc. If VHS 1256 b is actually at 20 pc, its place on the color-magnitude diagram would move up closer to the absolute magnitude of PSO 318.5.



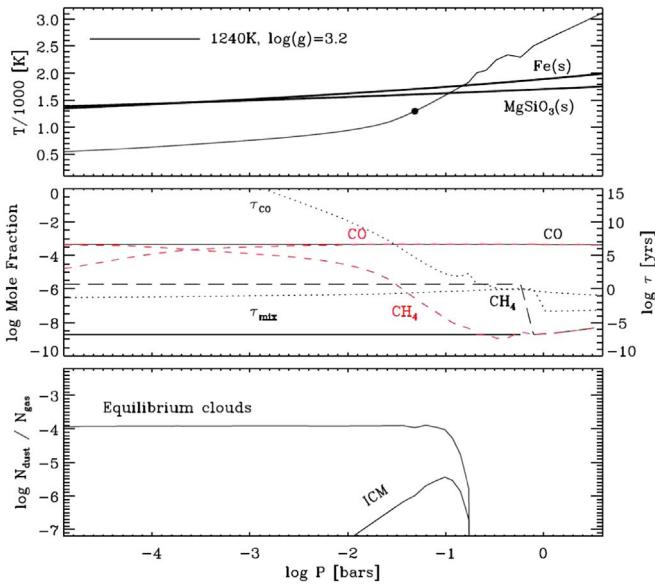


**Figure 7.** Atmospheric properties for VHS 1256 b and PSO 318.5. Top: temperature vs. pressure profile. The black dot approximates the location of the photosphere, and the condensation curves of enstatite ( $\text{MgSiO}_3$ ) and iron (Fe) are represented as thick black lines. Middle: CO and  $\text{CH}_4$  mole fractions for equilibrium (dashed, red), non-equilibrium (solid, black, with  $K_{zz}$  of  $10^8 \text{ cm}^2 \text{ s}^{-1}$ ) chemistry, and best-fit non-equilibrium with enhanced  $\text{CH}_4$  (dashed, black, with  $K_{zz}$  of  $10^8 \text{ cm}^2 \text{ s}^{-1}$ ). Chemical and mixing timescales are also plotted (dotted lines). Bottom: dust to gas ratio for the intermediate cloud model (ICM), used for the best-fit and the pure equilibrium cloud model.

Constraints on the distance and age of VHS 1256 b will allow for evolutionary constraints and a comparative analysis on the atmospheric properties and evolution of red, dusty objects. A summary of our best-fit and previously published parameters for VHS 1256 b and PSO 318.5 are shown in Table 2, along with parameters for similar objects.

## 5. Discussion

### 5.1. Strong Vertical Mixing in VHS 1256 b and PSO 318.5

In Section 4.1, we showed that VHS 1256 b and PSO 318.5 have less  $L$ -band methane absorption than similar-temperature brown dwarfs. This is evidence that their photospheres are not in chemical equilibrium. Strong vertical mixing can lower the amount of methane visible in the infrared spectra of low-gravity brown dwarfs and exoplanets (Hubeny & Burrows 2007; Barman et al. 2011b, 2015). Methane’s cross section per volume peaks at  $3.3 \mu\text{m}$ ; therefore,  $L$ -band spectra provide excellent constraints on methane abundances and vertical mixing.

A relatively high eddy diffusion coefficient was needed in our models ( $K_{zz} = 10^8 \text{ cm}^2 \text{ s}^{-1}$ ) to match the depths of the  $3.3 \mu\text{m}$  methane features. Assuming mixing length theory and that all of the convective flux from heat transport is contributing to mixing, the upper limit on  $K_{zz}$  is expected to range from  $10^8 \text{ cm}^2 \text{ s}^{-1}$  to  $10^9 \text{ cm}^2 \text{ s}^{-1}$  for low gravity, self-luminous, gas giant planets (Zahnle & Marley 2014).

### 5.2. Comparison with 3–4 $\mu\text{m}$ Photometry of HR 8799 c and d

As color–magnitude analogs of HR 8799 c and d, the spectra of VHS 1256 b and PSO 318.5 provide insight into the methane abundances and vertical mixing of these exoplanetary atmospheres. Using the  $L/M$ -band mid-InfraRed Camera

(LMIRcam) on the Large Binocular Telescope, Skemer et al. (2014) took adaptive optics corrected images of the HR 8799 system in six different custom narrowband filters. The images resulted in 3–4  $\mu\text{m}$  photometry of HR 8799 c and d. The NIRSPEC  $L$ -band spectra of VHS 1256 b and PSO 318.5 are convolved with the filters used in Skemer et al. (2014) to get synthetic photometry for comparison with HR 8799 c and d. In Figure 9, we show the normalized photometry of VHS 1256 b, PSO 318.5, and HR 8799 c and d, along with 2MASS J0559–1404, a  $\sim 1000 \text{ K}$ , T5 brown dwarf. The photometry for VHS 1256 b, PSO 318.5, and HR 8799 c and d is relatively flat, but there are slight differences. The spectral slopes of HR 8799 c and d start to decrease in flux past the  $3.59 \mu\text{m}$  photometry point, whereas the spectral slopes for VHS 1256 b and PSO 318.5 increase across the entire  $L$ -band. This may be due to slightly different cloud or temperature–pressure properties between these objects. Across  $3.31 \mu\text{m}$ , the spectral slopes of VHS 1256 b and PSO 318.5 appear as straight lines due to their weak methane signatures. HR 8799 c and d show a slight depression at the  $3.31 \mu\text{m}$  photometry point, which indicates that they may have more photospheric methane and weaker vertical mixing than VHS 1256 b and PSO 318.5. VHS 1256 b, PSO 318.5, and HR 8799 c and d all have less methane absorption relative to 2MASS J0559–1404 despite having similar photospheric temperatures, which indicates that all four objects are out of chemical equilibrium. In previous works by Hinz et al. (2010) and Skemer et al. (2014), non-equilibrium chemistry and photospheric clouds were needed to fit the near-infrared and mid-infrared photometry of HR 8799 c and d, and our model analysis on analogs VHS 1256 b and PSO 318.5 is consistent with this view.

### 5.3. Using $L$ -band spectroscopy to Detect Methane in Exoplanets and Brown Dwarfs

If strong vertical mixing is present on numerous young, gas giant exoplanets,  $L$ -band spectroscopy will be able to measure methane abundances for a wider range of objects at  $L$ -to- $T$  transition temperatures than near-infrared spectroscopy alone. The best-fit model from Section 4.3 was calculated with different  $\text{CH}_4$  mixing ratios above the quenching point. For each of those models, we calculated three separate reduced  $\chi^2$  values, only considering spectra within the MKO  $H$ -band, MKO  $K$ -band, and the extent of our  $L$ -band data. In Figure 10, the reduced  $\chi^2$  value versus the  $\text{CH}_4$  mixing ratio is plotted for the  $H$ -,  $K$ -, and  $L$ -band data of VHS 1256 b and PSO 318.5. The  $L$ -band produces a more prominent local minimum along the methane mixing ratio curve than the  $H$ - and  $K$ -bands, showing that methane was detected and the abundance in VHS 1256 b and PSO 318.5 can be constrained.

The methane feature at  $\sim 3.3 \mu\text{m}$  eventually blends in with the continuum at very low abundances when observed at lower resolutions (Figure 11). Future  $L$ -band observations that will study methane at similarly low abundances need to be done at resolutions of  $\sim 200$  or higher in order to detect methane. Medium- to high-resolution slit spectroscopy of isolated or wide companion brown dwarfs can be done from the ground at the  $L$ -band with a number of instruments on medium- to large-size telescopes (e.g., NIRSPEC, SpeX, iSHELL, CRIRES, and GNIRS; McLean et al. 1998; Rayner et al. 2003, 2016; Kaeuffl et al. 2004; Elias et al. 2006). Present-day integral field units (IFUs) that are focused on finding and characterizing

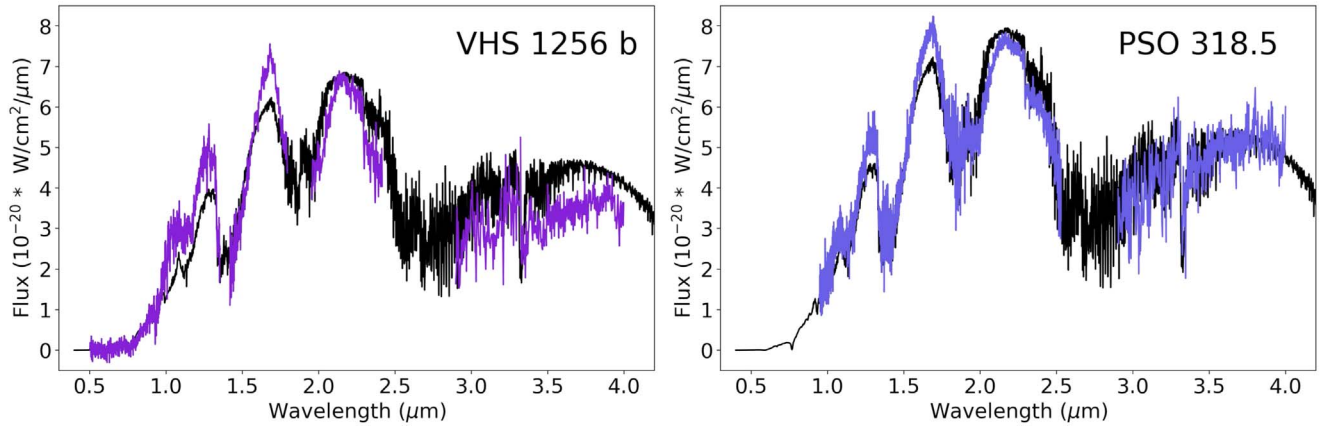


**Figure 8.** Near-infrared and  $L$ -band spectra for VHS 1256 b and PSO 318.5. The near-infrared spectra for VHS 1256 b and PSO 318.5 are from Gauza et al. (2015) and Liu et al. (2013). The best-fit, low-gravity ( $\log g = 3.2$ ), 1240 K model is shown in black in both panels.

**Table 2**  
Atmospheric Parameters of Low-gravity Objects

Object	$T_{\text{eff}}$ (K)	$\log g$	Radius ( $R_{\text{Jup}}$ )	$K_{\text{zz}}$ ( $\text{cm}^2 \text{s}^{-1}$ )	References
<b>VHS 1256 b</b>	<b>1240</b>	<b>3.2</b>	<b>0.9</b>	<b><math>10^8</math></b>	<b>1</b>
VHS 1256 b	800–1000	3.5–4.5	1.34–1.8	N/A	2, 3
<b>PSO 318.5</b>	<b>1240</b>	<b>3.2</b>	<b>1.3</b>	<b><math>10^8</math></b>	<b>1</b>
PSO 318.5	1210	4.21	1.40	N/A	2
HR 8799 c	1100	3.5	1.40	$10^8$	5
HR 8799 d	1100	3.5	1.40	$10^8$	5
2M1207 b	1000	4.0	1.5	$10^8$	6

**Note.** The atmospheric properties of VHS 1256 b, PSO 318.5, and other low-gravity brown dwarfs and exoplanets for comparison. The parameters adopted in this work are bolded. The distance to VHS 1256 b is not well constrained; therefore, a range of parameters is presented for previously published work. The parameters for HR 8799 c and d are from the grid that gave the best fit for data across the 3–5  $\mu\text{m}$  range in Greenbaum et al. (2018). References: (1) this work, (2) Liu et al. (2013), (3) Rich et al. (2016), (4) Gauza et al. (2015), (5) Greenbaum et al. (2018), (6) Barman et al. (2011b).

exoplanets in the glare of their host stars mostly operate blueward of the  $L$ -band (e.g., SPHERE, GPI, CHARIS; Beuzit et al. 2008; Macintosh et al. 2014; Groff et al. 2017). Currently, there is one exoplanet-imaging IFU (ALES Skemer et al. 2015) capable of low-resolution  $L$ -band spectroscopy. Higher spectral resolutions at the  $L$ -band are possible with lenslet and lenslet/slicer IFUs (Skemer et al. 2018). Fiber injection units can be placed behind high-contrast imaging systems to obtain even higher spectral resolutions of exoplanets (Wang et al. 2016; Mawet et al. 2017).

#### 5.4. Future James Webb Space Telescope Observations

*JWST* will be able to obtain high-fidelity spectra of brown dwarfs across a broad wavelength range, including the  $L$ -band. *JWST* can constrain the abundances of important secondary gases (e.g.,  $\text{H}_2\text{O}$ ,  $\text{CO}$ ,  $\text{CH}_4$ ,  $\text{NH}_3$ ) for the entire temperature range of known brown dwarfs (Lodders & Fegley 2002). Medium-resolution spectra over a broad wavelength range will be critical for adequately defining and measuring the C/O ratios and metallicities for brown dwarfs and exoplanets. There is evidence for silicate condensates in L-to-T transition objects

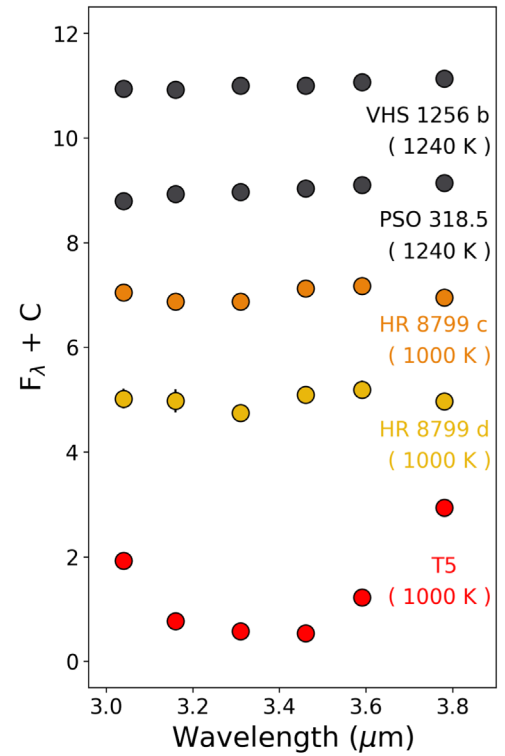


**Figure 9.** Top data points (black) are normalized 3–4  $\mu\text{m}$  photometry of VHS 1256 b and PSO 318.5 calculated using the narrowband filter profiles from Skemer et al. (2014). The temperatures of VHS 1256 b and PSO 318.5 are now derived from our model fits. The narrowband filter photometry for HR 8799 c and d are from Skemer et al. (2014) and are plotted as orange and yellow points. The narrowband photometry of 2MASS J0559–1404 (featured in Figure 4, from Cushing et al. 2005) is plotted in red. Relative to VHS 1256 b and PSO 318.5, HR 8799 c and d show deeper absorption at the 3.31  $\mu\text{m}$  photometry point, which suggests that they may have stronger methane absorption. However, the absorption is still shallower than that seen in the similar-temperature brown dwarf 2MASS J0559–1404, indicating that the HR 8799 c and d atmospheres are out of chemical equilibrium.

from *Spitzer* observations (Cushing et al. 2006), and it may be possible to determine the phase and composition of these silicates with Mid-Infrared Instrument (MIRI) spectra. Direct studies of condensates are important for testing our assumptions about clouds and the extent to which other physical effects (e.g., temperature instabilities, cloud microphysics) significantly influence the atmospheres of brown dwarfs



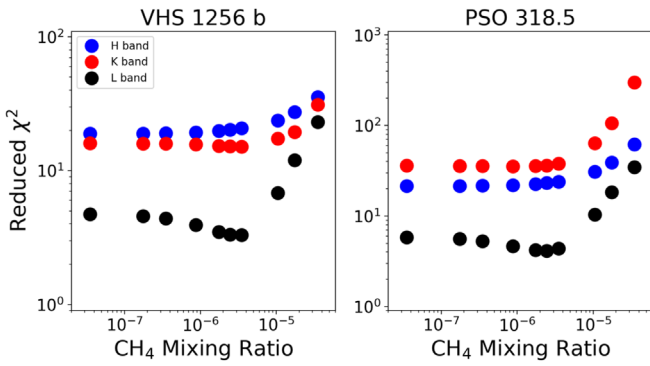


**Figure 10.** Reduced  $\chi^2$  value as a function of the  $\text{CH}_4$  mixing ratio for spectra within the MKO  $H$ -band (in blue), MKO  $K$ -band (in red), and our  $L$ -band spectra (black). The  $L$ -band curve has a more prominent local minimum that is not clearly seen at either the  $H$ - or  $K$ -band, allowing for the  $\text{CH}_4$  abundances to be constrained on VHS 1256 b and PSO 318.5. The models used for this analysis are the best-fit model with different  $\text{CH}_4$  mixing ratios.

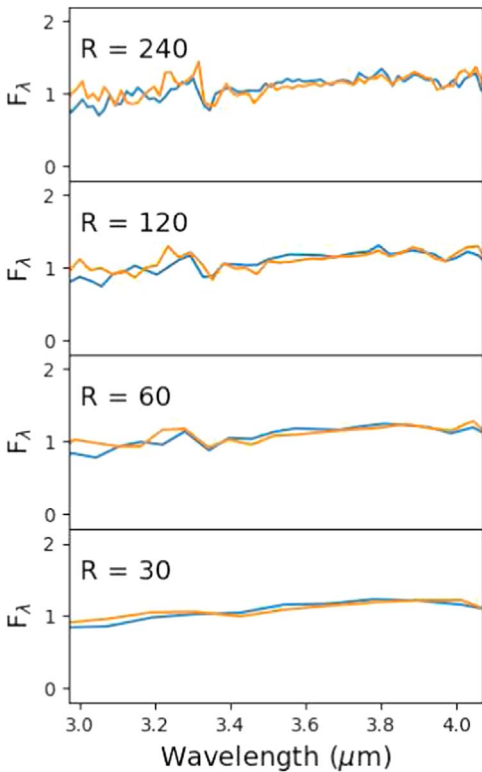


**Figure 11.**  $L$ -band spectra of PSO 318.5 (blue) and VHS 1256 b (orange) binned to different resolutions. The spectra are smoothed down with a boxcar kernel. Depending on the S/N of the detection, the Q-branch methane feature is hard to distinguish from the continuum below a resolution of  $\sim 200$ .

and exoplanets (Tremblin et al. 2017; Charnay et al. 2018; Leconte 2018).

Combining data from different epochs (as done in this work) may not accurately represent the average state of an atmosphere and introduces flux-calibration errors. Most brown dwarfs with time series photometric measurements appear variable at the few percent level and rotate on the order of hours (Biller 2017). PSO 318.5 has a measured variability of 3%–4% percent in several bands across the 1–5  $\mu\text{m}$  range, and these variations are suggested to be due to inhomogeneous cloud layers (Biller et al. 2015, 2018). No time series observations have been taken of VHS 1256 b. The

MKO and 2MASS  $J$ ,  $H$ , and  $K/K_s$  near-infrared photometry for PSO 318.5 are different by  $\sim 35\%$ ,  $\sim 9\%$ , and  $\sim 23\%$ , respectively. The same is also true for the VISTA and 2MASS  $J$ ,  $H$ , and  $K$  photometry of VHS 1256 b, which are different by  $\sim 37\%$ ,  $\sim 13\%$ , and  $\sim 3\%$ , respectively. The photometry of both objects are not completely inconsistent due to low S/N; however, they can lead to different colors and flux calibrations. This ultimately influences our interpretation of the atmospheric and evolutionary properties of both objects. *JWST*’s Near-Infrared Spectrograph (NIRSPEC) sensitivity enables contemporaneous coverage over the 1–5  $\mu\text{m}$  wavelength range, making spectroscopic monitoring of brown dwarfs feasible. Contemporaneous and precise, medium-resolution data of VHS 1256 b and PSO 318.5 will provide better constraints on the average effective temperature and other atmospheric properties of both objects.

#### 5.4.1. High Contrast Imaging of Exoplanets and Exoplanetary Early Release Science Program

The High Contrast Imaging of Exoplanets and Exoplanetary Systems with *JWST* Early Release Science (ERS) Program will utilize all of *JWST*’s instruments to provide a useful data set for the astronomical community to assess *JWST*’s ability to execute observations of exoplanetary systems (Hinkley et al. 2017). VHS 1256 b is the first choice target for NIRSPEC and MIRI IFU mode observations that will provide the first medium-resolution ( $R > 1000$ ), 0.7–28.0  $\mu\text{m}$  spectrum of an exoplanet analog.

The ERS spectrum will detect the majority of VHS 1256 b’s luminosity; important carbon-, oxygen-, and nitrogen-bearing gases; and silicate condensates if present. The resolution of the ERS spectrum is sufficient for detecting the methane features presented in this work and other minor/low-abundance molecular absorbers. The spectrum will be able to constrain all of the important carbon- and oxygen-bearing gases required to make an estimate for the C/O ratio of VHS 1256 b.

For gaseous solar system planets, the  $K_{zz}$  profile of an object may change relatively quickly over a scale height or yield different results depending on which non-equilibrium gases are measured (Smith 1998; Lellouch et al. 2002). NIRSPEC and MIRI measurements of CO and  $\text{CH}_4$  at multiple wavelengths can test the strength and vertical extent of  $K_{zz}$  along an assumed pressure versus temperature profile for VHS 1256 b. The ERS spectrum will be an enormous leap in the quality of data we have to study a directly imaged exoplanet analog, and will allow us to test, compare, and improve the array of models and retrievals used to characterize the atmospheres of brown dwarfs and exoplanets.

## 6. Summary and Conclusions

Low-gravity objects like 2MASS 1207 b and the HR 8799 planets appear redder on the color–magnitude diagram relative to field brown dwarfs. Their near-infrared spectra lack strong signatures of methane, hinting that these atmospheres are out of chemical equilibrium. This non-equilibrium chemistry can be explained by vertical mixing exchanging warm carbon-monoxide-rich gas with cool methane-rich gas. The opacity of methane is greatest within the  $L$ -band and dominates over other secondary gases such as carbon monoxide and water, making it an excellent wavelength region for constraining methane in low-gravity L-to-T transition objects.

In this work, we detect methane in  $R \sim 1300$ ,  $L$ -band spectra of the planetary-mass companion VHS 1256 b, and the young, free-floating, planetary-mass object PSO 318.5, which share the same color space as the HR 8799 planets. The  $L$ -band spectra of these two objects provide an early look into the composition and cloud properties of self-luminous, gas giant exoplanets that we can characterize with large ground-based telescopes in the future.

The results of this paper are as follows:

1. We detect low abundances of  $\text{CH}_4$  in  $L$ -band spectra of VHS 1256 b and PSO 318.5. Both objects have spectral slopes that are relatively flat, similar to the  $3\text{ }\mu\text{m}$ – $4\text{ }\mu\text{m}$  photometry of HR 8799 c and d featured in Skemer et al. (2014). HR 8799 c and d have deeper troughs through  $3.3\text{ }\mu\text{m}$ , suggesting that these planets have more methane and/or less vertical mixing than VHS 1256 b and PSO 318.5.
2. The reduced quantities of  $\text{CH}_4$  detected in VHS 1256 b and PSO 318.5 suggest non-equilibrium chemistry between CO and  $\text{CH}_4$ . The upper atmospheres of the best-fit models depart from equilibrium abundances of  $\text{CH}_4$  by factors of 10–100. An eddy diffusion coefficient ( $K_{zz}$ ) of  $10^8\text{ cm}^2\text{ s}^{-1}$  is required to match the depths of the  $3.3\text{ }\mu\text{m}$   $\text{CH}_4$  features.
3. The best-fit model to VHS 1256 b and PSO 318.5 is a low-gravity, 1240 K object with photospheric clouds. This model produces a reasonable radius for PSO 318.5 that is consistent with evolution models (Baraffe et al. 1998). VHS 1256 b’s spectrum looks remarkably similar to PSO 318.5; however, its uncertain distance manifests as an unconstrained radius. Future distance and age measurements will be able to connect these objects and others from an evolutionary standpoint.
4. Medium-resolution,  $L$ -band spectroscopy can detect low abundances of  $\text{CH}_4$  at  $3.3\text{ }\mu\text{m}$  even when the  $\text{CH}_4$  abundances are too low to be detectable at  $1.6\text{ }\mu\text{m}$  in medium-resolution  $H$ -band spectra. For objects similar to VHS 1256 b and PSO 318.5,  $R \sim 200$  is necessary to detect  $\text{CH}_4$  at the  $L$ -band.

All known directly imaged exoplanets fall within the temperature range of brown dwarfs. A handful of brown dwarfs even share the same infrared colors as exoplanets, and they are incredibly useful laboratories for studying the variety of atmospheric abundances and processes that are likely to be seen on gas giant exoplanets.

The authors wish to recognize and acknowledge the very significant cultural role and reverence that the summit of Maunakea has always had within the indigenous Hawaiian community. We are conducting observations from this mountain, which is colonized land. This work benefited from the Exoplanet Summer Program in the Other Worlds Laboratory (OWL) at the University of California, Santa Cruz, a program funded by the Heising-Simons Foundation. This work was funded by the NSF Planetary Astronomy, awards 1614320 and 1614492. J.M.S. is supported by NASA through Hubble Fellowship grant HST-HF2-51398.001-A awarded by the Space Telescope Science Institute, which is operated by the Association of Universities for Research in Astronomy, Inc., for NASA, under contract NAS5-26555. T.S.B. is supported by NSF AAG awards 1405505 and 1614492, and NASA XRP

award NNX17AB63G. B.E.M. would like to thank Gregg Dopman for answering questions about NIRSPEC; Bartek Gauza, who re-reduced the VHS 1256 b near-infrared spectra for our analysis; M. Buffaloe for reminding me to be my authentic self; and Solange Knowles for creating *A Seat at the Table*.

**Software:** Astropy, a community-developed core Python package for Astronomy (The Astropy Collaboration et al. 2018), Matplotlib (Hunter 2007), SciPy (Jones et al. 2001), Numpy (Van Der Walt et al. 2011), and Python 2.7.10.

## ORCID iDs

Brittany E. Miles  <https://orcid.org/0000-0002-5500-4602>  
 Andrew J. Skemer  <https://orcid.org/0000-0001-6098-3924>  
 Travis S. Barman  <https://orcid.org/0000-0002-7129-3002>  
 Katelyn N. Allers  <https://orcid.org/0000-0003-0580-7244>  
 Jordan M. Stone  <https://orcid.org/0000-0003-0454-3718>

## References

- Ackerman, A. S., & Marley, M. S. 2001, *ApJ*, **556**, 872  
 Allers, K. N., Gallimore, J. F., Liu, M. C., & Dupuy, T. J. 2016, *ApJ*, **819**, 133  
 Asplund, M., Grevesse, N., Sauval, A. J., & Scott, P. 2009, *ARA&A*, **47**, 481  
 Baraffe, I., Chabrier, G., Allard, F., & Hauschildt, P. H. 1998, *A&A*, **337**, 403  
 Barman, T. S., Konopacky, Q. M., Macintosh, B., & Marois, C. 2015, *ApJ*, **804**, 61  
 Barman, T. S., Macintosh, B., Konopacky, Q. M., & Marois, C. 2011a, *ApJ*, **733**, 65  
 Barman, T. S., Macintosh, B., Konopacky, Q. M., & Marois, C. 2011b, *ApJL*, **735**, L39  
 Beuzit, J.-L., Feldt, M., Dohlen, K., et al. 2008, *Proc. SPIE*, **7014**, 701418  
 Biller, B. 2017, *AstRv*, **13**, 1  
 Biller, B. A., Vos, J., Bonavita, M., et al. 2015, *ApJL*, **813**, L23  
 Biller, B. A., Vos, J., Buenzli, E., et al. 2018, *AJ*, **155**, 95  
 Bowler, B. P., Liu, M. C., Dupuy, T. J., & Cushing, M. C. 2010, *ApJ*, **723**, 850  
 Burgasser, A. J., Marley, M. S., Ackerman, A. S., et al. 2002, *ApJL*, **571**, L151  
 Burrows, A., Marley, M., Hubbard, W. B., et al. 1997, *ApJ*, **491**, 856  
 Burrows, A., Sudarsky, D., & Hubeny, I. 2006, *ApJ*, **640**, 1063  
 Charnay, B., Bézard, B., Baudino, J. L., et al. 2018, *ApJ*, **854**, 172  
 Chauvin, G., Lagrange, A.-M., Dumas, C., et al. 2004, *A&A*, **425**, L29  
 Currie, T., Burrows, A., Girard, J. H., et al. 2014, *ApJ*, **795**, 133  
 Currie, T., Burrows, A., Itoh, Y., et al. 2011, *ApJ*, **729**, 128  
 Cushing, M. C., Rayner, J. T., & Vacca, W. D. 2005, *ApJ*, **623**, 1115  
 Cushing, M. C., Roellig, T. L., Marley, M. S., et al. 2006, *ApJ*, **648**, 614  
 Dupuy, T. J., & Liu, M. C. 2012, *ApJS*, **201**, 19  
 Elias, J. H., Joyce, R. R., Liang, M., et al. 2006, *Proc. SPIE*, **6269**, 62694C  
 Faherty, J. K., Rice, E. L., Cruz, K. L., Mamajek, E. E., & Núñez, A. 2013, *AJ*, **145**, 2  
 Foreman-Mackey, D., Hogg, D. W., Lang, D., & Goodman, J. 2013, *PASP*, **125**, 306  
 Gauza, B., Béjar, V. J. S., Pérez-Garrido, A., et al. 2015, *ApJ*, **804**, 96  
 Geballe, T. R., Knapp, G. R., Leggett, S. K., et al. 2002, *ApJ*, **564**, 466  
 Golimowski, D. A., Leggett, S. K., Marley, M. S., et al. 2004, *AJ*, **127**, 3516  
 Greenbaum, A. Z., Pueyo, L., Ruffio, J.-B., et al. 2018, *AJ*, **155**, 226  
 Groff, T., Chilcote, J., Brandt, T., et al. 2017, *Proc. SPIE*, **10400**, 1040016  
 Guzmán-Marmolejo, A., & Segura, A. 2015, *Boletín de la Sociedad Geológica Mexicana*, **67**, 377  
 Hinkley, S., Skemer, A., Biller, B., et al. 2017, in *High Contrast Imaging of Exoplanets and Exoplanetary Systems with JWST*, JWST Proposal ID 1386 (Baltimore, MD: STScI), <https://jwst.stsci.edu/observing-programs/approved-ers-programs/program-1386>  
 Hinz, P. M., Rodigas, T. J., Kenworthy, M. A., et al. 2010, *ApJ*, **716**, 417  
 Hubeny, I., & Burrows, A. 2007, *ApJ*, **669**, 1248  
 Hunter, J. D. 2007, *CSE*, **9**, 90  
 Jones, E., Oliphant, T., Peterson, P., et al. 2001, *SciPy: Open Source Scientific Tools for Python*, <http://www.scipy.org/>  
 Kaeufli, H.-U., Ballester, P., Biereichel, P., et al. 2004, *Proc. SPIE*, **5492**, 1218  
 Karkoschka, E. 1994, *Icar*, **111**, 174  
 Kepler, F., Hamilton, J. T. G., Braß, M., & Röckmann, T. 2006, *Natur*, **439**, 187  
 Kirkpatrick, J. D. 2005, *ARA&A*, **43**, 195  
 Knapp, G. R., Leggett, S. K., Fan, X., et al. 2004, *AJ*, **127**, 3553

- Konopacky, Q. M., Barman, T. S., Macintosh, B. A., & Marois, C. 2013, *Sci*, **339**, 1398
- Leconte, J. 2018, *ApJL*, **853**, L30
- Lellouch, E., Bézard, B., Moses, J. I., et al. 2002, *Icar*, **159**, 112
- Liu, M. C., Dupuy, T. J., & Allers, K. N. 2016, *ApJ*, **833**, 96
- Liu, M. C., Magnier, E. A., Deacon, N. R., et al. 2013, *ApJL*, **777**, L20
- Lodders, K., & Fegley, B. 2002, *Icar*, **155**, 393
- Lunine, J. I. 1993, *ARA&A*, **31**, 217
- Macintosh, B., Graham, J. R., Ingraham, P., et al. 2014, *PNAS*, **111**, 12661
- Madhusudhan, N., Burrows, A., & Currie, T. 2011, *ApJ*, **737**, 34
- Marley, M. S., Saumon, D., Cushing, M., et al. 2012, *ApJ*, **754**, 135
- Marois, C., Macintosh, B., Barman, T., et al. 2008, *Sci*, **322**, 1348
- Marois, C., Zuckerman, B., Konopacky, Q. M., Macintosh, B., & Barman, T. 2010, *Natur*, **468**, 1080
- Mawet, D., Delorme, J. R., Jovanovic, N., et al. 2017, *Proc. SPIE*, **10400**, 1040029
- McLean, I. S., Becklin, E. E., Bendiksen, O., et al. 1998, *Proc. SPIE*, **3354**, 566
- Metchev, S., Marois, C., & Zuckerman, B. 2009, *ApJL*, **705**, L204
- Morley, C. V., Marley, M. S., Fortney, J. J., et al. 2014, *ApJ*, **787**, 78
- Noll, K. S., Geballe, T. R., Leggett, S. K., & Marley, M. S. 2000, *ApJL*, **541**, L75
- Öberg, K. I., Murray-Clay, R., & Bergin, E. A. 2011, *ApJ*, **743**, L16
- The Astropy Collaboration, Price-Whelan, A. M., Sipőcz, B. M., et al. 2018, arXiv:1801.02634
- Rayner, J., Tokunaga, A., Jaffe, D., et al. 2016, *Proc. SPIE*, **9908**, 990884
- Rayner, J. T., Toomey, D. W., Onaka, P. M., et al. 2003, *PASP*, **115**, 362
- Rich, E. A., Currie, T., Wisniewski, J. P., et al. 2016, *ApJ*, **830**, 114
- Rieke, G. H., Blaylock, M., Decin, L., et al. 2008, *AJ*, **135**, 2245
- Saumon, D., & Marley, M. S. 2008, *ApJ*, **689**, 1327
- Skemer, A. J., Close, L. M., Szűcs, L., et al. 2011, *ApJ*, **732**, 107
- Skemer, A. J., Hinz, P., Montoya, M., et al. 2015, *Proc. SPIE*, **9605**, 96051D
- Skemer, A. J., Hinz, P. M., Esposito, S., et al. 2012, *ApJ*, **753**, 14
- Skemer, A. J., Marley, M. S., Hinz, P. M., et al. 2014, *ApJ*, **792**, 17
- Skemer, A. J., Stelter, D., Mawet, D., et al. 2018, arXiv:1808.03304
- Smith, M. D. 1998, *Icar*, **132**, 176
- Stone, J. M., Skemer, A. J., Kratter, K. M., et al. 2016, *ApJL*, **818**, L12
- Tremblin, P., Chabrier, G., Baraffe, I., et al. 2017, *ApJ*, **850**, 46
- Tsuji, T., & Nakajima, T. 2003, *ApJL*, **585**, L151
- Van Der Walt, S., Colbert, S. C., & Varoquaux, G. 2011, *CSE*, **13**, 22
- Wang, J., Mawet, D., Hu, R., & Benneke, B. 2016, *Proc. SPIE*, **9911**, 99112T
- Wright, E. L., Eisenhardt, P. R. M., Mainzer, A. K., et al. 2010, *AJ*, **140**, 1868
- Yurchenko, S. N., & Tennyson, J. 2014, *MNRAS*, **440**, 1649
- Zahnle, K. J., & Marley, M. S. 2014, *ApJ*, **797**, 41